Research Square

Preprints are preliminary reports that have not undergone peer review.
They should not be considered conclusive, used to inform clinical practice,
or referenced by the media as validated information.

Photocatalytic degradation of Methyl Orange under ultraviolet-visible light irradiation using WO3-ZnO nanocomposites synthesized via Saffron petal extract

Reza Irankhah
semnan university
Ali Balooch
semnan university
Hassan Koohestani
h.koohestani@semnan.ac.ir

semnan university

Article

Keywords: WO3-ZnO Nanocomposite, Green Synthesis, Photocatalysis, Dye Degradation

Posted Date: July 1st, 2026

DOI: https://doi.org/10.21203/rs.3.rs-9779730/v1

License: This work is licensed under a Creative Commons Attribution 4.0 International License.
Read Full License

Additional Declarations: No competing interests reported.

Version of Record: A version of this preprint was published at Scientific Reports on September 26th, 2026. See the published version at https://doi.org/10.1038/s41598-026-72803-5.

Photocatalytic degradation of Methyl Orange under ultraviolet-visible light irradiation using WO_3-ZnO nanocomposites synthesized via Saffron petal extract

Reza Irankhah[a*], Ali Balooch[b], Hassan Koohestani[b**]

[a] Department of Ceramics, Faculty of Materials and Metallurgical Engineering, Semnan University, Semnan, Iran

[b] Faculty of Materials and Metallurgical Engineering, Semnan University, Semnan, Iran

*r.irankhah@semnan.ac.ir

**h.koohestani@semnan.ac.ir

Abstract

The elimination of organic dyes through photocatalysis is an effective approach for achieving pollution-free environments. WO_3-ZnO nanocomposites with ZnO:WO_3 weight ratios of 100:0, 80:20, 60:40, 40:60, 20:80, and 0:100, labeled as 100Z, 20WZ, 40WZ, 60WZ, 80WZ, and 100W, respectively, were synthesized through an environmentally green synthesis method. Subsequently, the WO_3-ZnO nanocomposites were utilized for the photocatalytic degradation of methyl orange (MO) under the irradiation of ultraviolet -visible light. The resultant products were characterized using a comprehensive suite of characterization techniques, including X-ray diffraction (XRD), Brunauer-Emmett-Teller (BET), field emission scanning electron microscopy (FESEM), energy dispersive spectroscopy (EDS), dynamic light scattering (DLS), Fourier transform infrared spectroscopy (FTIR), and diffuse reflectance spectroscopy (DRS). The XRD patterns indicated the formation of crystal structures of ZnO, WO_3, and the WO_3-ZnO nanocomposites. Based on optical investigations, the direct optical band gaps of 100Z, 20WZ, 40WZ, 60WZ, 80WZ, and 100W were measured to be 3.29, 3.27, 3.09, 3.26, 3.05, and 2.99 eV, respectively. The photocatalytic efficacy of the synthesized nanocomposites was evaluated through the degradation of MO. The obtained results demonstrated that the synergistic effect between WO_3 and ZnO contributes to the enhancement of the charge separation and reduction in the recombination rates of charge carriers, thereby significantly augmenting the photocatalytic efficiency. Notably, the 40WZ nanocomposite exhibited the highest photocatalytic degradation efficiency of MO under UV -vis light irradiation. It was observed that 100% degradation of the MO dye could be achieved by the 40WZ nanocomposite within 15 min of light irradiation.

Keywords: WO_3-ZnO Nanocomposite, Green Synthesis, Photocatalysis, Dye Degradation.

1. Introduction

In recent decades, significant population growth and subsequent increase in industrial production have been among the main factors contributing to the production of physical and biological pollutants on Earth [1]. Human culture is truly undermined by the consistently expanding use of natural resources, particularly fresh water, and man is compelled to fix the dirtied water to save his environment on Earth [2]. The chemical pollution of water has become a considerable concern all around the world. Anthropogenic sources of water contamination consist of organic and inorganic substances. Cationic Methylene blue, Methyl orange, rhodamine B, fuchsine, and anionic Congo red dyes are among the pollutants found in industrial wastewater [3-5]. The dyes generally have a complex structure and high molecular weight, are water soluble, difficult to degrade, and are carcinogenic in nature [3-5]. Among these dyes, methyl orange (MO) is distinguished as a prominent pollutant due to its extensive use in various industries, including textiles, printing, and pharmaceuticals [6]. Therefore, numerous conventional systems, including chemical, physical, and biological systems, have been developed for the treatment of polluted water [7-12]. Traditional techniques have many limitations, including high energy consumption, low efficiency, and toxic byproducts [13]. Therefore, environmentally friendly advanced photocatalytic processes using semiconductors are used to treat wastewater [14]. Semiconductors have gained more attention from researchers due to their unique crystal structure, tunable surface morphology, and intrinsic catalytic property. Despite the good catalytic properties of semiconductors, their short hole diffusion length and recombination of charge carriers reduce their degradation efficiency [15]. Therefore, a catalyst to be used in degradation must fulfill the defined criterion, such as an appropriate band gap, chemical stability, and effective electron-hole pair separation [16]. Various semiconductors, such as TiO_2 and ZnO, have been widely investigated as photocatalysts in pollutant degradation [17].

ZnO is an important semiconductor photocatalyst with a direct band gap of approximately 3.37 eV [18]. ZnO exhibits high photocatalytic capability, chemical stability, and high electron mobility [19]. Nevertheless, ZnO presents two main drawbacks during the photocatalytic process owing to its wide band gap: (i) its operational range is restricted to only the UV region ($\lambda \leq 400$ nm), which is less than 5% of the entire solar spectrum, and (ii) the relatively high electron – hole recombination rate [18, 20]. One of the ways to overcome these problems is to modify ZnO by adding another semiconductor (ZnO-SnO_2, ZnO-CdS, ZnO-CeO_2, ZnO-TiO_2) [18, 21-23]. Therefore, by coupling different semiconductors, the band gap of ZnO can be

reduced, and its absorption range can be extended to the visible light region. Additionally, the electron-hole pair separation can be promoted under visible light irradiation, resulting in increased photocatalytic activity [18]. The unique physical, chemical, and biological properties of WO_3 semiconductors make them a cost-effective option for photocatalytic applications [24]. Despite this advantage, WO_3 semiconductors possess a relatively low conduction band potential, which limits their ability to generate superoxide radicals through the interaction between conduction band electrons and oxygen molecules during photodegradation processes [25].

Tungsten oxide is a multifunctional n-type semiconductor with a low band gap energy of 2.4-2.8 eV[20] that exhibits unusual electronic and optoelectronic character [26]. Hybridizing ZnO with WO_3 can form a more negative conduction band level, which can promote the separation of photo-induced carriers and photodegradation activity [17, 26]. Various synthesis methods have been reported for preparing WO_3-ZnO composites. For example, Changlin et al. have synthesized WO_3-ZnO composites via precipitation-grinding and calcination methods and used them for the photocatalytic degradation of acid orange II under UV light irradiation [27]. Adhikari et al. have synthesized WO_3-ZnO composites for dye degradation under visible light. They found that the mixed oxide of WO_3 and ZnO with an optimum amount of 1:9 achieves 90% degradation of methylene blue and orange G dye [28]. Hunge et al. prepared WO_3-ZnO thin films via a simple spray pyrolysis technique for the degradation of phthalic acid from polluted waters. The WO_3-ZnO thin films enhanced phthalic acid degradation under visible light [29]. Hunge et al. investigated the structural, morphological, and compositional properties of WO_3 and WO_3-ZnO nanocomposites for the sonocatalytic degradation of brilliant blue dye. WO_3-ZnO nanocomposites exhibit maximum sonocatalytic activity compared to the WO_3 photocatalyst [30]. Lei et al. investigated the photocatalytic performance of ZnO nanoparticle-modified WO_3 nanosheet arrays under solar light illumination. In particular, the 30-WZ nanocomposite exhibited superior photocatalytic efficiency [17]. Mugunthan et al. reported the visible-light-irradiated photocatalytic degradation of diclofenac using WO_3-ZnO catalysts, which were prepared by the hydrothermal method. The ZnW10 catalyst was an efficient photocatalyst with 76% mineralization of diclofenac under visible-light illumination [31]. AgI/WO_3/ZnO nanocomposite was synthesized for the photodegradation of methylene blue by Ghattavi et al. The optimal mole ratio for the best performance was 2:1:1, and the resulting composite removed approximately 79% of the MB in the aqueous solution during the 40-min photodegradation process [32]. Chaudhary et al. synthesized ternary WO_3-ZnO@rGO

nanocomposites. The results indicated that graphene oxide improved charge carrier transfer in photocatalysts. Moreover, 94% dye removal was achieved in 90 min under visible light irradiation [20]. ZnO nanorods and nanowires based ZnO/WO_3/Pt heterojunction were successfully synthesized by Yasir et al. via the hydrothermal growth method. The heterojunctions achieved an excellent photodegradation rate in the range of 23-37% and 63-86% for nanorod and nanowire morphologies, respectively [33]. Radhi et al. prepared WO_3-ZnO nanocomposites using a hydrothermal method [34]. Mokhtar et al. synthesized WO_3-ZnO composite photocatalyst via chemical precipitation. Bisphenol A degradation in aqueous solution under visible light irradiation achieved the best degradation percentage of 65.73% within 180 min [26]. Zhang et al. investigated the photocatalytic degradation of oxytetracycline using WO_3-ZnO catalysts synthesized by the precipitation method. The results showed that the composite had the best photocatalytic activity when the ratio of WO_3 to ZnO was 1:3 [35]. Aziz et al. synthesized WO_3, ZnO, and WO_3-ZnO nanocomposite using co-precipitation and ultrasonication, respectively, as an effective photocatalyst for removing rhodamine B and methylene blue under visible light. The degradation percentages of methylene blue and rhodamine B were 94% and 85.7%, respectively [36]. Ternary NH_2-GO/ZnO-WO_3 composite prepared by the solvothermal method. The photocatalytic degradation results indicate that the ternary photocatalyst demonstrated superior photocatalytic efficiency toward methylene blue (85.89%) compared to NH_2-GO/ZnO (52.28%) under UV light irradiation [37]. Farsi et al. prepared Mo-doped WO_3-ZnO nanocomposites loaded with polyvinyl alcohol via a simple mixing method to decompose methyl orange. It has been shown that 92% of methyl orange dye is degraded under visible light [38]. Xie et al. have prepared WO_3-ZnO composites via a low-temperature aqueous route. The degradation of methyl orange in an aqueous solution was used to evaluate the performance of the as-prepared WO_3-ZnO composites[18].

Based on the related literature, there are various papers related to the photocatalytic dye degradation of WO_3-ZnO composites, but the number of biological and especially green synthesis studies is limited. The biological method of synthesizing nanocomposites is a valuable alternative to traditional chemical synthesis methods, offering a fast, environmentally friendly, and cost-effective technique. In one study, Rani et al. synthesized ZnO-WO_3 nanocomposite via facile precipitation and green synthesis method by employing M. koenigii plant extract. They investigated the photodegradation of bisphenol A and auramine O under sunlight irradiation [39]. To the best of our knowledge, this study represents the first report related to the green synthesis methodology of WO_3-ZnO nanocomposites as a photocatalyst for

methyl orange degradation using UV-vis irradiation. In this study, the green synthesis of WO_3-ZnO nanocomposites was performed using saffron petal extract (SPE) as a reducing and stabilizing agent. A series of WO_3-ZnO nanocomposites with different WO_3 contents was successfully prepared via green synthesis. Their photocatalytic activity was evaluated by the decomposition of MO in aqueous solution. .

2. Experimental methodology

2.1. Materials

Zinc nitrate hexahydrate (98.5%) and WO_3 (99%, extra pure) were used as the zinc and tungsten sources, respectively. Ammonia solution (25%) (EMSURE grade product) was used as a pH-adjusting agent. The methyl orange (MO) dye was obtained from the DRM laboratory and pharmaceutical chemicals, Iran.

2.2 Preparation of saffron petal extract (SPE)

Saffron petals were collected from Sarayan, South Khorasan Province, Iran. A specific number of saffron petals was soaked in 500 mL of distilled water for 15 min to prepare the extract. The resulting mixture was then boiled for 1 hour at 100 °C. After cooling, the solution was filtered and centrifuged at 8000 rpm for 5 min to remove coarse particles.

2.3. Preparation of WO_3-ZnO nanocomposites

The precipitation method was employed for the preparation of WO_3–ZnO photocatalysts. Initially, a certain amount of WO_3 was dissolved in 50 mL of SPE extract. Then, a specific amount of $Zn(NO_3)_2 \cdot 6H_2O$ was dissolved in 20 mL of distilled water and added dropwise to the same solution. Subsequently, ammonia solution was gradually added until the pH reached 10. The resulting mixture was magnetically stirred for 1 h, and the formed precipitates were washed several times with distilled water. The obtained precipitates were dried at 100 °C for 60 min and finally calcined at 450 °C for 2 h. The WO_3–ZnO nanocomposites with different weight ratios of ZnO to WO_3 (100:0, 80:20, 60:40, 40:60, 20:80, and 0:100) were synthesized following the same procedure. The resulting samples were labeled as 100Z, 20WZ, 40WZ, 60WZ, 80WZ, and 100W, respectively. Fig. 1 illustrates the green synthesis process of the WO_3–ZnO nanocomposites using SPE.

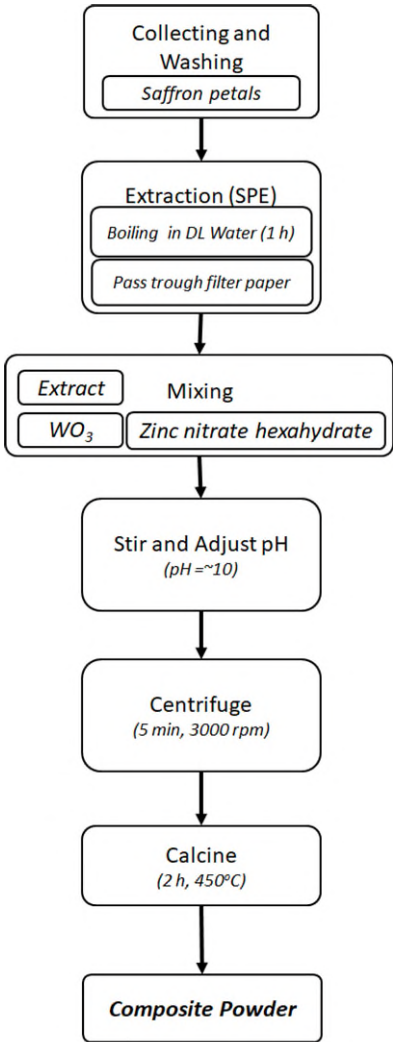

Fig. 1. Schematic diagram for the synthesis of WO_3-ZnO nanocomposites using SPE.

2.4. Characterization methods

The XRD data and phase evaluation of the photocatalysts were obtained using an X-ray diffractometer (Bruker D8) equipped with Cu-Kα radiation (λ = 1.5418 Å). The specific surface area and porosity characteristics were analyzed using the BET method with a BELSORP-MiniX instrument. The surface morphologies were observed using a field emission scanning electron microscope (FESEM, CIQTEK-EM5000X). Energy dispersive X-ray analysis (EDX) was employed to determine the elemental composition on the surface of the photocatalysts. The particle size distribution was measured by dynamic light scattering (DLS) using a Malvern Nano-ZS90 instrument .Fourier transform infrared (FTIR) spectra were recorded using a PerkinElmer spectrometer. Ultraviolet–visible diffuse reflectance spectra (UV–vis DRS) were

obtained in the wavelength range of 200–900 nm using an S4100 SCINCO spectrophotometer to investigate the optical absorption properties and determine the band gap energy .

2.5. Photodegradation of Methyl Orange (MO)

The photocatalytic activity of WO_3-ZnO nanocomposites for the removal of methyl orange (MO) from an aqueous solution with an initial concentration of 100 ppm was investigated. For this purpose, 50 mL of MO solution was treated with 0.1 g of the synthesized nanocomposites in a Pyrex batch reactor under UV irradiation from a 500 W xenon lamp, positioned 13 cm above the solution surface. Samples were collected at 5, 15, and 30 min. To enhance the photocatalytic process, 3 drops of hydrogen peroxide (H_2O_2) as a reactive oxygen species were slowly added to the above mixture at room temperature. The photocatalytic degradation efficiency (%) was calculated using the intensities of the optical absorption spectra of the unirradiated (I_0) and irradiated (I_t) samples as follows [40]:

$$\text{Degradation efficiency (\%)} = ((I_0-I_t)/(I_0)) \times 100 \quad (1)$$

3. Results and discussion

3.1. X-ray diffraction study

The XRD patterns of pure ZnO, pure WO_3, and WO_3-ZnO nanocomposites with different WO_3 contents are shown in Fig. 2. The XRD spectra of the synthesized ZnO show diffraction peaks at 2θ = 31.73, 34.37, 36.21, 47.48, 56.53, 62.77, 66.30, 67.86, 69.00, 72.46, and 76.86, indicating a typical hexagonal crystal structure with crystallographic planes of (100), (002), (101), (102), (110), (103), (200), (112), (210), (004), and (202), respectively (JCPDS card No. 01-089-1397). The diffraction peaks of WO_3 can be well indexed to the monoclinic phase of WO_3 (JCPDS card No. 00-002-0308). Furthermore, the XRD spectra of WO_3-ZnO photocatalysts show WO_3 and ZnO diffraction peaks, confirming the simultaneous presence of both WO_3 and ZnO in the nanocomposites.

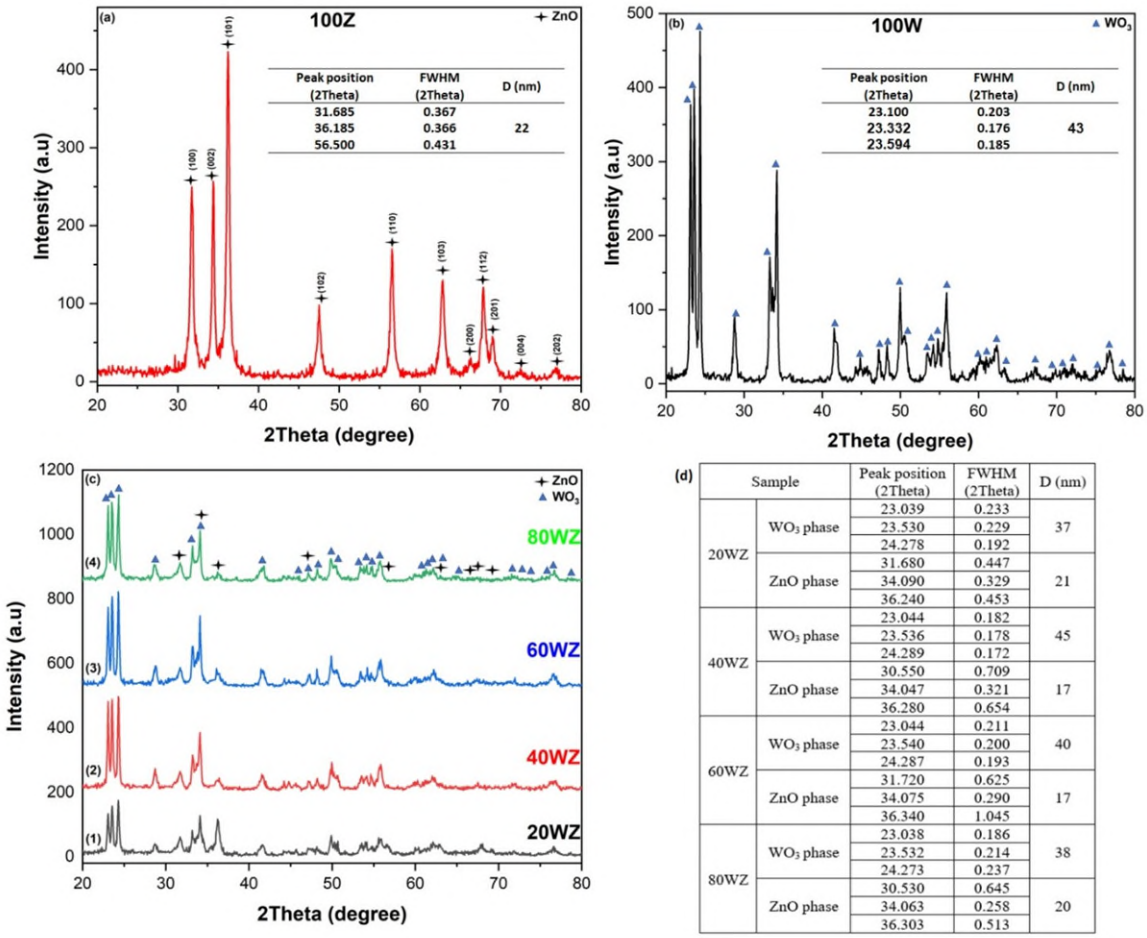

(d)

Sample		Peak position (2Theta)	FWHM (2Theta)	D (nm)
20WZ	WO_3 phase	23.039	0.233	37
		23.530	0.229	
		24.278	0.192	
	ZnO phase	31.680	0.447	21
		34.090	0.329	
		36.240	0.453	
40WZ	WO_3 phase	23.044	0.182	45
		23.536	0.178	
		24.289	0.172	
	ZnO phase	30.550	0.709	17
		34.047	0.321	
		36.280	0.654	
60WZ	WO_3 phase	23.044	0.211	40
		23.540	0.200	
		24.287	0.193	
	ZnO phase	31.720	0.625	17
		34.075	0.290	
		36.340	1.045	
80WZ	WO_3 phase	23.038	0.186	38
		23.532	0.214	
		24.273	0.237	
	ZnO phase	30.530	0.645	20
		34.063	0.258	
		36.303	0.513	

Fig. 2. XRD of synthesized (a) 100Z, (b) 100W, (c) WO_3-ZnO nanocomposites, and (d) crystallite size of WO_3-ZnO nanocomposites.

According to the XRD analysis in Fig. 2, no characteristic peaks from impurities were detected. The crystallite size (D) of the samples was calculated using X-ray line broadening by Scherrer's formula ($D=0.9\lambda/\beta Cos(\theta)$), where D denotes the average crystallite size, λ=1.5418 Å the wavelength of the Cu Kα line, β is the full width at half maximum (FWHM) for the corresponding peak, and θ is Bragg's diffraction angle [32]. The mean crystallite size of the 100Z and 100W was 22 and 43 nm, respectively. The mean crystallite size of the 20WZ, 40WZ, 60WZ, and 80WZ samples is summarized in a table (Fig. 2d). The results show that the addition of WO_3 increased the mean crystallite size of the pure ZnO. Increasing the crystallite size decreases the specific surface area and hence decreases the photocatalytic degradation rate [41].

3.2. BET surface area analysis

Fig. 3 shows the nitrogen adsorption–desorption isotherms (ADS and DES) for different samples. As observed from the shape of the curves, all samples exhibit a sharp increase in the adsorbed volume at high relative pressures (P/P_0 close to 1), which is characteristic of a type IV isotherm according to the IUPAC classification, indicating the presence of a mesoporous structure in the materials. Furthermore, the presence of a hysteresis loop between the adsorption and desorption branches confirms the existence of open pores and complex pore geometries, such as interconnected or ink-bottle-like pores. At lower relative pressures ($P/P_0 < 0.35$), a linear region of the isotherm is observed, which is used for BET calculations. From this region, the specific surface area of the samples can be calculated by plotting the BET equation and determining the monolayer volume (V_m) and the constant C. Based on a qualitative comparison of the curves, samples with a higher adsorption volume over the entire pressure range possess larger specific surface areas and greater pore volumes. For example, the WZ-labeled samples exhibit stronger adsorption behavior than the 100W and 100Z samples, which may be attributed to a more favorable pore size distribution and an increased number of active surface sites.

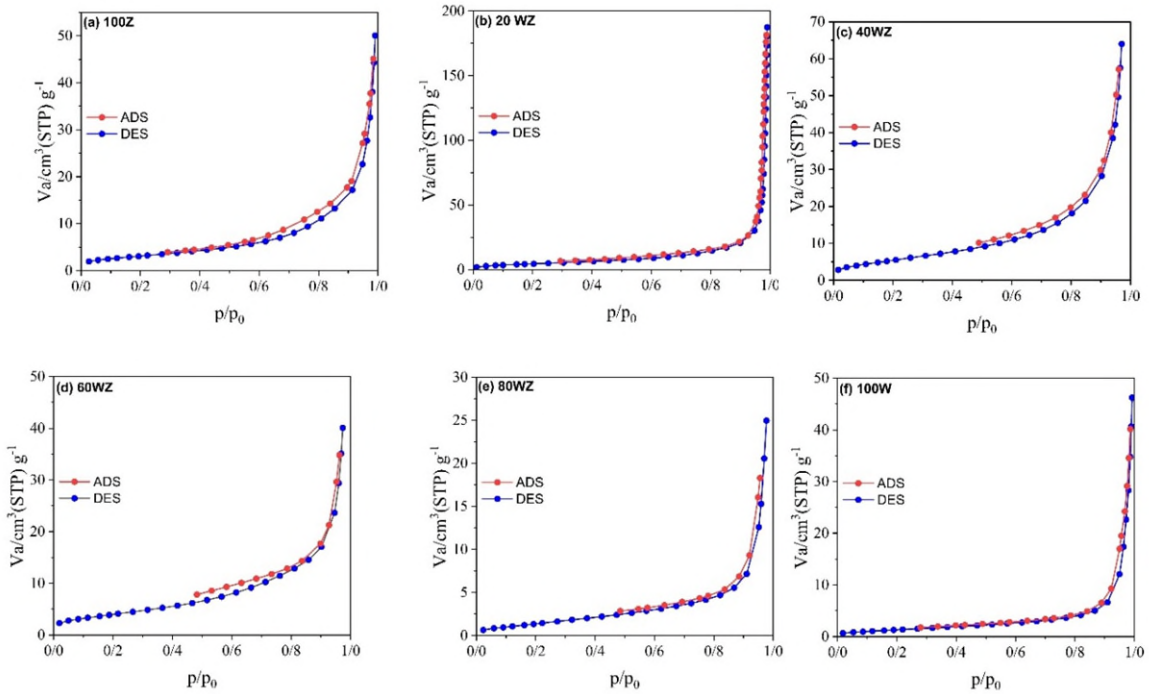

Fig. 3. Nitrogen adsorption-desorption isotherms of (a) 100Z, (b) 20WZ, (c) 40WZ, (d) 60WZ, (e) 80WZ, and (f) 100W.

Table 1 shows the textural properties of the photocatalysts. BET analysis of the synthesized samples revealed significant differences in surface area, pore volume, and pore size among pure WO_3, pure ZnO, and WO_3-ZnO nanocomposites. The 40WZ nanocomposite exhibited the highest specific surface area (20.413 m^2/g) and total pore volume (0.99023 cm^3/g) with a moderate mean pore diameter of 19.404 nm, indicating abundant active sites and good accessibility to pollutant molecules. Intermediate nanocomposites, such as 20WZ and 60WZ, also showed relatively high surface areas and pore volumes, providing favorable conditions for photocatalytic activity. In contrast, pure WO_3 (100W) had the lowest surface area (3.9680 m^2/g) and pore volume (0.064357 cm^3/g), limiting its adsorption capacity, whereas pure ZnO (100Z) had a large pore diameter (27.74 nm) with moderate surface area and pore volume. Overall, the BET results indicate that nanocomposites with moderate WO_3 content, particularly 40WZ, possess optimal textural properties for enhanced photocatalytic degradation due to their combination of high surface area, suitable pore volume, and appropriate pore size. In a study by He et al. [42], WO_3-ZnO nanocomposites with varying WO_3 ratios showed different BET characteristics that significantly influenced their photocatalytic performance. In another investigation by Xu et al. [43], WO_3-ZnO nanocomposites with different surface areas exhibited varying efficiencies in the photocatalytic degradation of pollutants. Zhang et al. [35] also demonstrated that WO_3-ZnO nanocomposites with different WO_3 contents possessed distinct BET properties that affected their photocatalytic activity. Finally, Ashiegbu et al. [44] showed that ZnO-[10%]WO_3 nanocomposites with a specific surface area of 5.69 m^2/g exhibited high photocatalytic activity in pollutant degradation.

Table. 1: Textural properties of all the prepared photocatalysts by BET analysis.

Samples	**V_m [cm^3(STP) g^{-1}]**	**a_s [m^2 g^{-1}]**	**Mean pore diameter [nm]**	**BET C constant**	**Total pore volume [cm^3. g^{-1}]**
100 Z	2.5025	10.898	27.740	106.54	0.075536
20 WZ	3.6853	16.040	71.600	55.459	0.287100
40 WZ	4.6899	20.413	19.404	68.797	0.990230
60 WZ	3.1063	13.520	18.336	110.05	0.061978
80 WZ	1.3666	5.9481	25.964	17.492	0.038609
100 W	0.9117	3.9680	64.877	135.68	0.064357

3.3. Morphological study

The FE-SEM images presented in Fig. 4 illustrate the morphology of pure WO_3, pure ZnO, and WO_3–ZnO nanocomposites with different weight ratios. As shown in Fig. 4f, the WO_3 nanoparticles (100W) exhibit a layered or sheet-like structure densely stacked together, with an average particle size of 95–130 nm. This morphology is typical of WO_3, which often forms nanosheet- or nanorod-like structures .In the 20WZ sample (Fig. 4b), which contains a low percentage of WO_3, a cauliflower-like morphology characteristic of ZnO is dominant, while WO_3 appears as fine nanosheets distributed on the surface of ZnO particles. This structure enhances the interfacial contact area between the ZnO and WO_3 phases, resulting in better adhesion and stronger interparticle interactions.

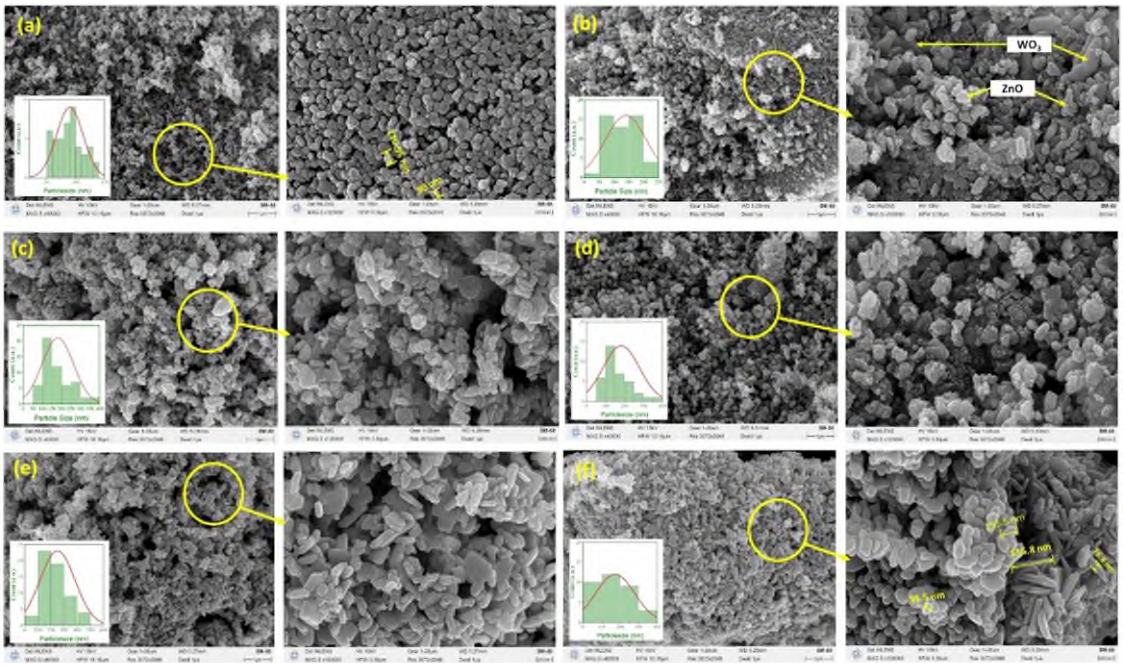

Fig. 4. FE-SEM images of the synthesized samples: (a) 100Z, (b) 20WZ, (c) 40WZ, (d) 60WZ, (e) 80WZ, and (f) 100 W, at magnifications of 40,000× and 100,000×.

For the 40WZ and 60WZ nanocomposites (Figs. 4c and 4d), as the WO_3 content increases, the particles become more uniformly dispersed, and a mixed morphology composed of rod-like and cauliflower-shaped structures was observed. In these samples, WO_3 nanoparticles are homogeneously deposited on the ZnO surface, which can promote efficient charge transfer and improve photocatalytic performance. The average particle size in these nanocomposites is

estimated to be approximately 100–150 nm .In the 80WZ sample (Fig. 4e), due to the higher content of WO_3, most of the surface is covered by WO_3 particles, leading to partial agglomeration, which could reduce the available active surface area. Finally, the pure ZnO sample (100Z, Fig. 4a) exhibited a distinct cauliflower-like morphology with densely packed spherical particles sized approximately 80–120 nm. This morphology is consistent with previous reports for ZnO nanoparticles synthesized via green, aqueous solution, and solvothermal methods [45-47].

The SEM micrograph in Fig. 5 shows the surface morphology of the 40WZ nanocomposite at high magnification (×100,000). Two distinct regions, marked as (a) and (b), are highlighted to represent the WO_3-rich and ZnO-rich areas, respectively. In region (a), the particles exhibited a rod- or plate-like morphology, which is characteristic of WO_3 structures. These particles appear densely packed, corresponding to the tungsten oxide phase identified in the EDS spectrum. In contrast, region (b) shows spherical and loosely aggregated particles, typically attributed to ZnO, which provide a higher surface area and facilitate enhanced photocatalytic activity. The corresponding EDS spectra confirm the elemental composition of each region. For region (a), the strong peaks of W and O with weight percentages of 82.84% (W) and 17.16% (O) confirm the formation of WO_3. For region (b), the dominant peaks of Zn and O, with weight percentages of 82.08% (Zn) and 17.92% (O), indicate the presence of ZnO. Minor Au peaks originate from the gold coating used to improve sample conductivity during SEM imaging. Overall, the SEM–EDS results confirm the successful synthesis and homogeneous distribution of both WO_3 and ZnO phases within the nanocomposite. The distinct morphologies of WO_3 (rod-like) and ZnO (spherical) are expected to promote efficient charge separation and improve photocatalytic performance through enhanced interfacial contact.

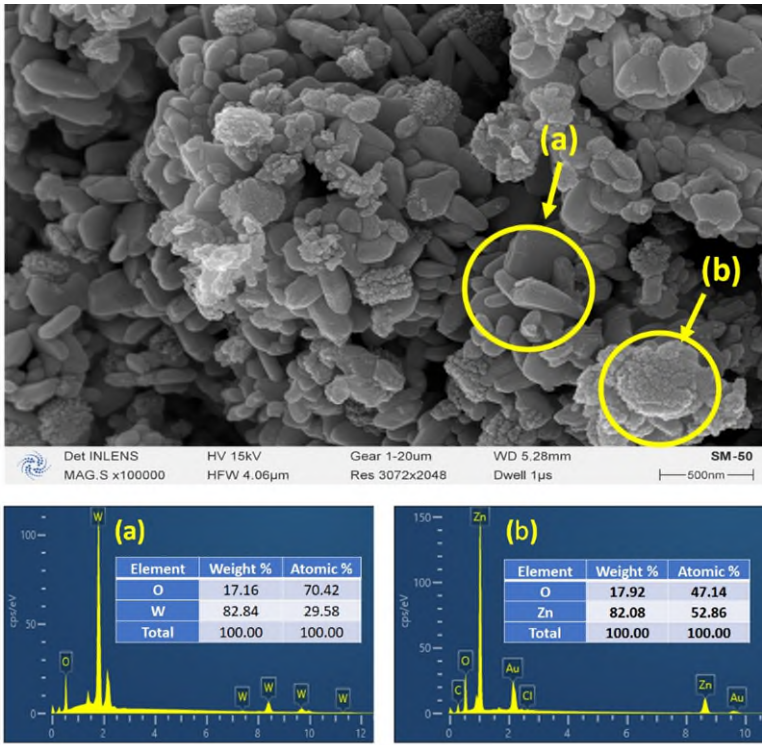

Fig. 5. EDS spectrum of 40WZ (100WO_3 (a) and 100ZnO (b)).

According to the DLS results (Fig. 6), the average particle size and the width of their distribution change systematically with varying WO_3 content, indicating that the composition ratio significantly influences the dispersion behavior in the liquid medium. The particle size distribution in the pure ZnO sample (100Z) primarily falls within the range of 80-700 nm, with an average hydrodynamic diameter of approximately 250-300 nm. This broad distribution suggests partial agglomeration of particles in the aqueous medium, which can be attributed to the high surface energy of ZnO nanoparticles and the strong van der Waals forces between them. With the addition of a small amount of WO_3 (sample 20WZ), the DLS curve shifts toward larger sizes (500-3500 nm), indicating the formation of loose agglomerates. This behavior may result from the surface charge heterogeneity between ZnO and WO_3 phases, leading to electrostatic attraction and the formation of mixed particle clusters. As the WO_3 content increases to 40 and 60 wt.% (samples 40WZ and 60WZ), the particle size distribution narrows, and the average hydrodynamic diameter decreases to approximately 500-900 nm. This trend reflects improved dispersion stability and uniform particle distribution within the nanocomposites. The formation of heterogeneous junctions between WO_3 and ZnO likely enhances electrostatic repulsion among particles, preventing their re-agglomeration. Such

balanced structures typically result in smaller, more uniform particle distributions and improved suspension colloidal stability.

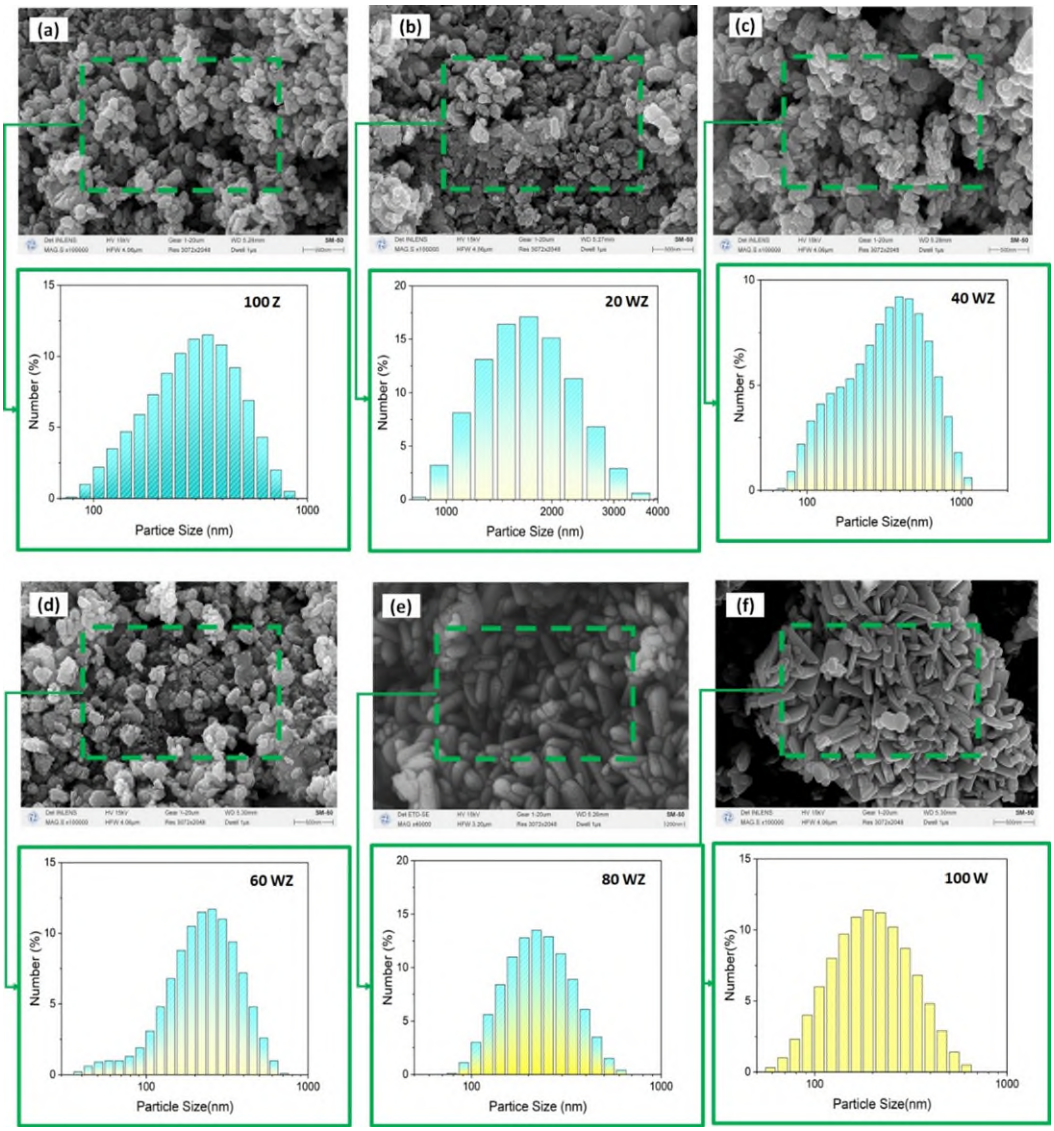

Fig. 6. DLS measurements of the size dispersion of the: (a) 100Z, (b) 20WZ, (c) 40WZ, (d) 60WZ, (e) 80WZ, and (f) 100W.

Although the DLS curve appears relatively narrow in the 80WZ sample and most particles fall within the 150-300 nm range, a tail extending toward larger sizes is observed, indicating partial agglomeration. Finally, for the pure WO_3 sample (100W), the DLS curve shows a symmetric distribution with a central peak around 200-400 nm, which is clearly larger than the particle sizes observed in the FE-SEM images. This discrepancy arises from the nature of DLS, which

measures the hydrodynamic diameter, including not only the particle core but also the surrounding hydrated layer and any molecules adsorbed from the synthesis medium. Overall, the DLS results consistently show larger particle sizes than the FE-SEM observations. This difference can be attributed to three main factors: (i) partial agglomeration of nanoparticles in the liquid medium, (ii) the presence of hydrated layers and adsorbed solvent or residual synthesis molecules, and (iii) the inherent sensitivity of DLS to light scattering intensity, which is disproportionately influenced by larger particles. Therefore, it can be concluded that increasing the WO_3 content up to approximately 60 wt.% improves the particle dispersion and colloidal stability of the WO_3/ZnO system, whereas higher contents (above 80 wt.%) lead to the onset of partial aggregation.

3.4. FT-IR analysis

The FT-IR spectra of SPE, 100Z, 20WZ, 40WZ, 60WZ, 80WZ, and 100W are shown in Fig. 7. The FT-IR spectrum of SPE indicates various functional groups. The broad and intense band around ~3400 cm^{-1} corresponds to the O–H stretching vibrations of phenolic and alcoholic groups, suggesting the presence of antioxidant compounds and hydrogen bonding. The peak observed at ~2920 cm^{-1} is attributed to the stretching vibrations of the C–H bonds in the alkyl groups, such as methyl and methylene. The band near ~1620 cm^{-1} may correspond to C=C stretching in aromatic structures or possibly secondary C=O groups. The well-defined band in the region of 1060–1100 cm^{-1} is due to C–O stretching vibrations, which are commonly associated with alcohols, sugars, or flavonoids. Finally, the weak peaks in the 600–800 cm^{-1} region are attributed to out-of-plane C–H bending in aromatic rings [48, 49].

The characteristic peaks of the 100Z sample are located at 445 and 3448 cm^{-1}. The absorption peak in the 3448 cm^{-1} is related to the bending and stretching vibration modes of the absorbed water (-OH groups) on the surface of the samples. The peak located at 445 cm^{-1} corresponds to the stretching vibration of the Zn-O bond [27, 50]. In the 20WZ sample, the peak at 445 cm^{-1} is the characteristic peak of ZnO, and this peak is sharp, which might be due to the high ZnO content in the sample. Because the WO_3 content increased and the ZnO content decreased, the peak value at 445 cm^{-1} decreased in 40WZ, 60WZ, 80WZ, and 100W. The characteristic peaks corresponding to 100W are located at 771, 825, and 3448 cm^{-1}. Furthermore, these peaks are similarly observed in the case of 20WZ, 40WZ, 60WZ, and 80WZ samples. The peak at approximately 771 cm^{-1} is attributed to the stretching vibrations of the W-O groups. Another peak, found around 825 cm^{-1}, is associated with the asymmetric vibration of the W-O bonds.

Additionally, a weak peak around 1680 cm^{-1} corresponds to the stretching vibration of the W=O bands [36, 51].

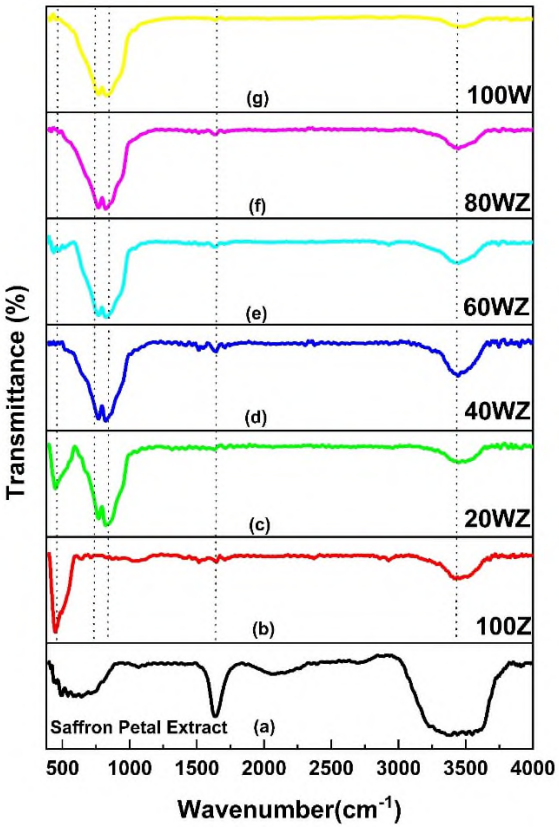

Fig. 7. FT-IR analysis of (a) SPE, (b) 100Z, (c) 20WZ, (d) 40WZ, (e) 60WZ, (f) 80WZ, and (g) 100W.

3.5. Optical studies

The optical properties of the as-synthesized 100Z, 100W, and WO_3-ZnO nanocomposites were investigated using UV-vis diffuse reflectance spectroscopy (DRS). The light absorption capability of the samples is shown in Fig. 8. The presence of only one absorption peak in the UV region signifies a high ZnO dispersion and superior interaction between ZnO and WO_3 particles [52]. As shown in Fig. 8a, pure ZnO has light absorption from 200 to 380 nm and almost no absorption in the visible light region. The presence of WO_3 resulted in a red shift of absorption toward longer wavelengths. The red shift increased with increasing WO_3 content. The 40WZ, 60WZ, 80WZ, and 100W samples exhibited a red shift in the visible light range compared with the pure 100Z. These findings indicate that the proficient absorption of light, which is associated with the transfer of electrons from the valence band to the conduction band,

can be ascribed to the shift of the WO_3-ZnO nanocomposite's absorption edge into the visible light region, thereby promoting the movement of photogenerated electrons and holes [43]. Additionally, the considerable reflectance band in the visible light region could be harnessed to facilitate the photodegradation of pollutants [17].

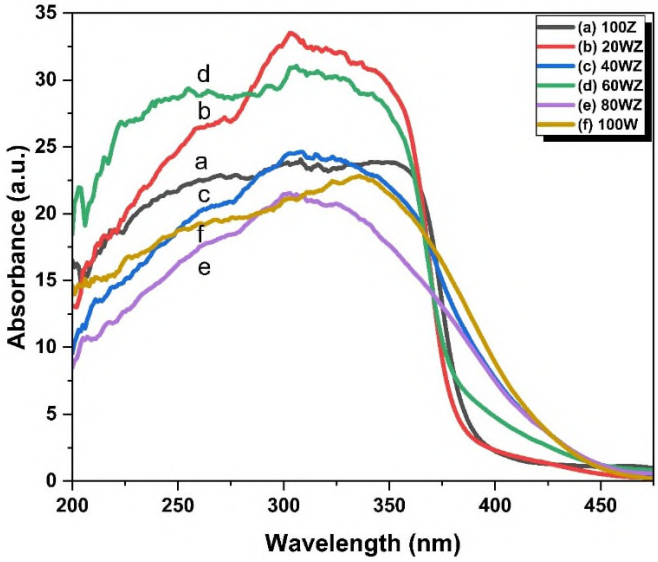

Fig. 8. UV-vis DRS spectra of (a) 100Z, (b) 20WZ, (c) 40WZ, (d) 60WZ, (e) 80WZ, and (f) 100W.

The band gap position of a semiconductor is one of the chief components for predicting its photocatalytic efficiency [20]. The direct and indirect band gaps of the as-synthesized samples were calculated using the modified Tauc equation, also known as the Kubelka-Munk equation ($F(R)=(1-R)^2/2R$), where R is the reflectance [53]. The band gaps of the samples were determined from the plot of $(h\upsilon F(R))^n$ vs $E=h\upsilon$, assuming that the absorption coefficient is proportional to the KM function $(h\upsilon F(R))^n$. The constant value n is related to the direct (n= 2) or indirect (n= 0.5) band gap [54]. According to some studies, ZnO and WO_3 are direct band gap materials with varying band gap energies [43]. However, some other researchers have reported that ZnO and WO_3 are indirect band gap materials [17]. The band gaps of the samples were obtained by extrapolating the linear part of the KM curve along the horizontal axis, which indicates the energy value of the photon ($E=h\upsilon$). The optical direct band gap values of pure ZnO, pure WO_3, 20WZ, 40WZ, 60WZ, and 80WZ samples were estimated approximately to be 3.29, 2.99, 3.27, 3.09, 3.26, and 3.05 eV, respectively, as shown in Fig. 9(a-f). The indirect band gap values were also calculated for the respective photocatalysts, which were 3.08, 2.55, 2.60, 2.48, 2.60, and 2.59 eV, respectively (given in the inset of Fig 9(a-f)). Pure WO_3 exhibits

a narrow band gap of approximately 2.55 eV compared to pure ZnO, which possesses a band gap of 3.08 eV. Consequently, the integration of appropriate ZnO and WO_3 semiconductor materials into a WO_3-ZnO nanocomposite has the potential to alter the forbidden band width of the composite and enhance its optical absorption capabilities within the visible light spectrum [43]. Thus, the resultant WO_3-ZnO nanocomposite enables the facilitation of electron transitions into the conduction band of ZnO, thereby increasing the light absorption efficiency of ZnO [43].

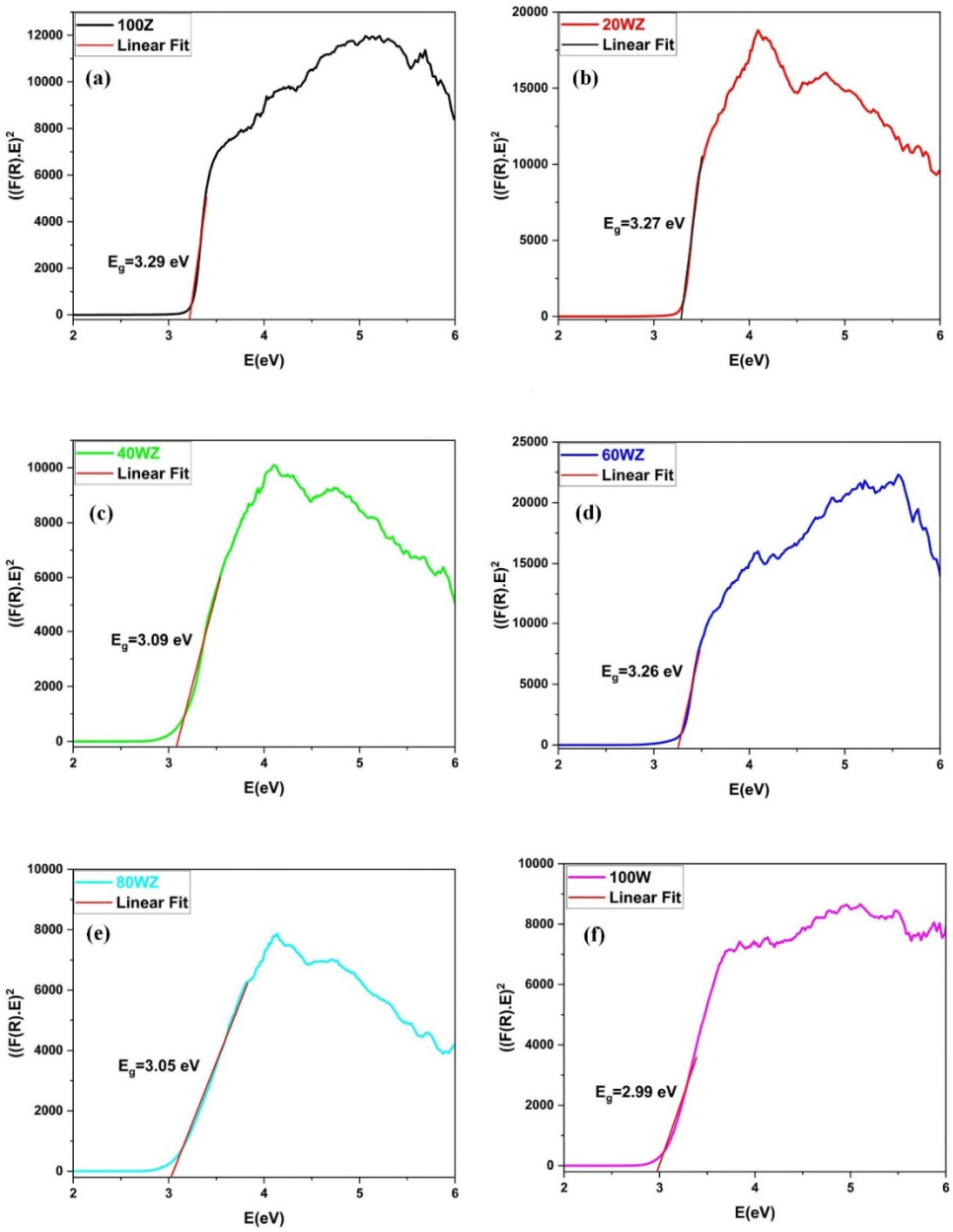

Fig. 9. Kubelka-Munk (KM) transform of DRS data for (a) 100Z, (b) 20WZ, (c) 40WZ, (d) 60WZ, (e) 80WZ, and (f) 100W.

3.6. Photocatalytic degradation

Fig. 10 shows the UV-vis time-dependent absorption spectra of the MO solution degradation under light and dark conditions in the presence of 100Z, 20WZ, 40WZ, 60WZ, 80WZ, and 100W samples. During the photocatalytic degradation experiments, the decrease in the absorbance peaks indicates a decrease in the MO concentrations. The gradual absorbance change of MO exposed to UV-vis irradiation for different time intervals at 5, 15, and 30 min clearly reflects the photocatalytic degradation rate of each sample. Pure ZnO and pure WO_3 exhibit weak photocatalytic degradation efficiency. The increase in WO_3 from 0 to 40 wt.% effectively increased the degradation efficiency. However, a further increase in WO_3 had an adverse effect. The optimal concentration of WO_3 was 40 wt.%. The 40WZ sample shows the most significant reduction in peak intensity, indicating the fastest degradation of MO, whereas 100Z (pure ZnO) exhibits much slighter decreases.

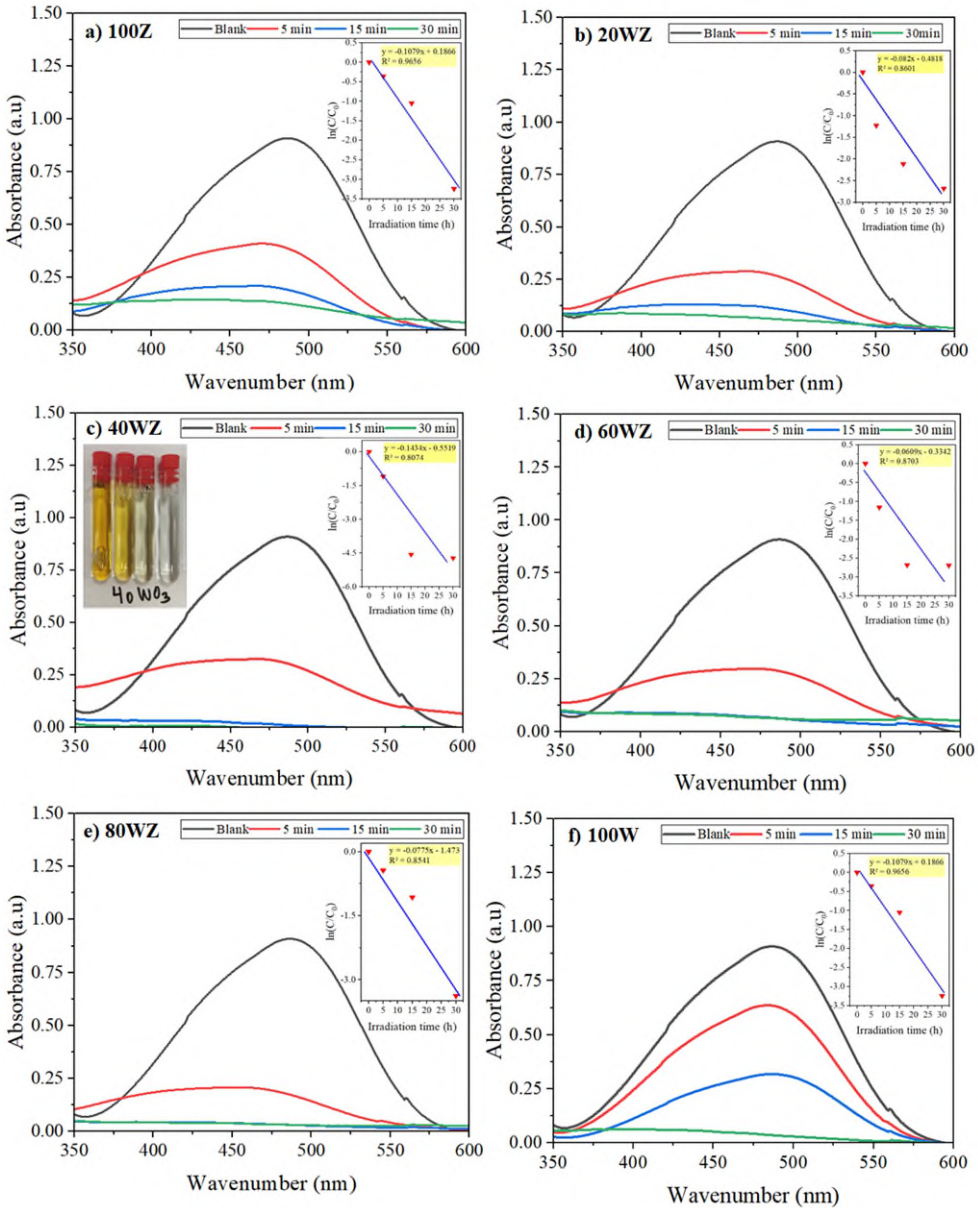

Fig. 10. UV-vis spectra of the MO degradation at different times of the light and dark conditions in the presence of (a) 100Z, (b) 20WZ, (c) 40WZ, (d) 60WZ, (e) 80WZ, and (f) 100W.

The reaction kinetics of the MO degradation is expressed by the pseudo-first-order equation ln $(C/C_0) = -k\ t$ [20], as shown in the insets of Fig. 10. Here, C_0 and C are the concentrations of MO in solution at time 0 and t, respectively, and the slope of these lines corresponds to the rate constant (k). Since the concentration of MO is proportional to its absorbance according to the Beer–Lambert law, the kinetic equation can be expressed as ln $(C_t/C_0) =$ ln (A_t/A_0), where C_0 and C_t are the initial and remaining concentrations of MO at time t, respectively, and A_0 and A_t denote the corresponding absorbance values measured at 487 nm. The methyl orange (MO)

degradation was calculated based on the decrease in absorbance intensity at 487 nm using the following equation:

$$\text{Degradation efficiency } (\%) = ((A_0 - A_t) / (A_0)) \times 100 \quad (2)$$

The 40WZ sample displays the highest slope (k), confirming that it follows pseudo-first-order kinetics very well. The photocatalytic degradation efficiency of WO_3-ZnO nanocomposite with different content of WO_3 for treatment of MO solution upon irradiation of UV-vis light is shown in Fig. 11. As can be shown, the WO_3-ZnO composites displayed better catalytic efficiency than pure WO_3 and pure ZnO. The results show that the 40WZ photocatalyst showed the highest performance, and MO was completely treated within 15 min.

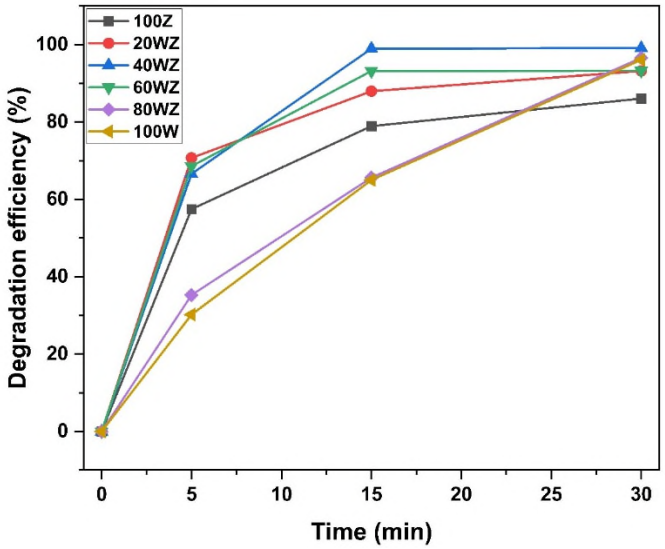

Fig. 11. Photocatalytic degradation efficiency of WO_3-ZnO nanocomposite with different content of WO_3.

Fig. 12 shows the photocatalytic degradation mechanism of MO dye using the WO_3-ZnO nanocomposites. The processes observed in Fig. 12 arise from three main factors: (1) the formation of an effective WO_3/ZnO heterojunction, which facilitates electron transfer from ZnO to WO_3 as predicted by the band alignment diagram; (2) enhanced production of reactive radicals such as $^{\bullet}OH$ and $^{\bullet}O_2^-$, which rapidly diminish the MO absorption peak (~487 nm); and (3) a balanced combination of band gap and particle size, leading to faster spectral decay during irradiation. Subsequently, these reactive species attack MO molecules, causing a rapid decline

in absorbance intensities and the strong linearity observed in the kinetic plots for the most efficient samples, particularly 40WZ.

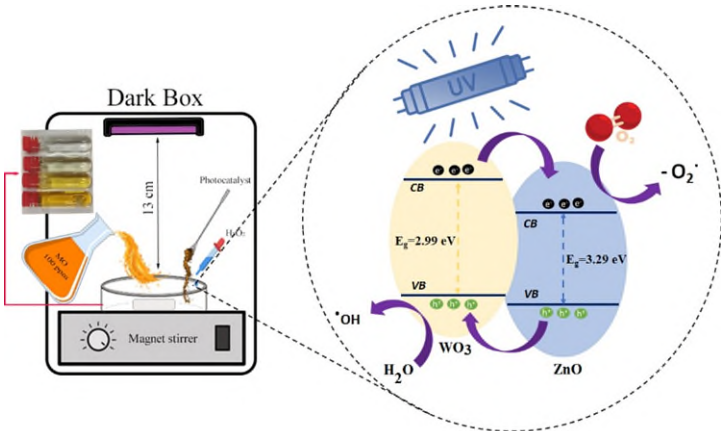

Fig. 12. Schematic of the photocatalytic mechanism of the WO_3-ZnO nanocomposite photocatalyst.

Based on the related literature, for the WO_3-ZnO nanocomposites, superoxide radicals ($^{\bullet}O_2^-$), holes (h^+), and hydroxyl radicals ($^{\bullet}OH$) have been identified as the main active species for the photo degradation of MO [17, 18, 42]. Upon UV-vis excitation, the photoexcited electrons of ZnO travel from the conduction band to that of WO_3 (Eq. 5), whereas the holes move in the reverse direction (Eq. 6). The electrons at the WO_3 conduction band can react with oxygen molecules adsorbed on the catalyst surface to form $^{\bullet}O_2^-$ (Eq. 7). These superoxide anions may either directly attack the MO or generate hydroxyl radicals. Moreover, the holes of the valence band of WO_3 can oxidize the adsorbed water or hydroxyl groups to produce $^{\bullet}OH$ radicals (Eq. 8). Additionally, the H_2O_2 can serve as an electron acceptor but also as a strong oxidizing agent that can decompose to $^{\bullet}OH$ radicals, which will substantially enhance the overall oxidative capacity of the system (Eq. 9).

Consequently, the degradation efficiency can be improved by suppressing the recombination of electron-hole pairs for efficient charge separation.

$$ZnO + h\nu \rightarrow e^- + h^+ \quad (3)$$

$$WO_3 + h\nu \rightarrow e^- + h^+ \quad (4)$$

$$e^-(ZnO) \rightarrow e^-(WO_3) \quad (5)$$

$$h^+(WO_3) \rightarrow h^+(ZnO) \quad (6)$$

$$e^- + O_2 \rightarrow {}^{\bullet}O_2^- \quad (7)$$

$$h^+ + H_2O \rightarrow {}^{\bullet}OH + H^+ \quad (8)$$

$MO + {}^{\bullet}OH + {}^{\bullet}O_2^- \rightarrow$ Degradated products (9)

Table 2 shows a comparison of the photocatalytic activity of WO_3-ZnO with previously reported studies for different dye degradations. The data analysis indicates that the photocatalytic performance of WO_3-ZnO nanocomposites depends on several key factors: the Zn-to-W molar ratio, the synthesis method, the type of light irradiation, and the band gap of the nanocomposite.

Nanocomposites such as ZnO–10%WO_3 prepared via the milling-calcination method can degrade nearly 64.5% of MO [42], whereas increasing the WO_3 content to 40 wt.% achieves complete MO degradation in just 15 min, highlighting the importance of precise component ratios and optimized synthesis conditions. The synthesis method also plays a crucial role; for instance, sonochemical synthesis of WO_3/ZnO enabled 90% degradation of Brilliant Blue in 40 min [55], while green synthesis approaches, such as ZnO/WO_3 under sunlight, achieved high removal efficiencies (96% AO and 91% BPA) [39]. The nanocomposite band gap is also significant; lower band gap values allow the use of a broader light spectrum and result in higher photocatalytic activity. For example, when PVA was added to the Mo-WO_3/ZnO nanocomposite, the band gap value reduced from 2.01 to 1.7 eV, resulting in a desirable photocatalytic performance [38]. Moreover, these nanocomposites are capable of simultaneously degrading multiple pollutants, such as WO_3-ZnO, removing MO, RhB, and BPA with varying efficiencies [42]. In summary, WO_3-ZnO nanocomposites, with optimized composition, appropriate synthesis method, and effective use of light, serve as versatile and efficient photocatalysts for the degradation of various organic pollutants in wastewater.

Table 2. The photocatalytic performance of the as-prepared photocatalysts is compared to that of other researchers.

Photocatalyst	**Synthesis Method**	**Light**	**Band Gap (eV)**	**Dye Degradation**	**Ref.**
Zn: W (10:1 molar ratio)	Hydrothermal	Visible light	2.8	Mineralization of 76% of diclofenac during the irradiation time of 270 min	[31]
ZnO/WO_3 (equal molar concentrations of ZnO and WO_3)	Green synthesis using M. koenigii leaves extract	Sunlight	2.3	Maximum degradation of AO (96%) and BPA (91%) during the irradiation time of 300 min	[39]

WO_3/ZnO	Sonochemical	Sonocatalytic	--	Degradation of 90% of Brilliant Blue after 40 min	[55]
ZnO-10% WO_3	Ball-milling + Calcination	UV light	--	MO= 64.5%, RhB=75.91%, BPA=62.02%	[42]
Mo-doped WO_3/ZnO@PVA	Simple mixing	Visible light	1.7	MO removal performance of 92% after 120 min	[38]
3 mol%WO_3/ZnO	Aqueous solution	UV–vis	--	MO was almost completely degraded within 180 min	[18]
WO_3-ZnO (40 wt.%WO_3)	Green synthesis	UV-vis	Direct: 3.09 Indirect: 2.48	~100% MO removal in 15 min	This study

4. Conclusion

ZnO, WO_3, and WO_3-ZnO nanocomposites were successfully prepared using the green synthesis method. The morphological, structural, and optical properties were identified by FESEM, XRD, and UV-vis absorption spectroscopy. Compared with pure ZnO and WO_3, WO_3-ZnO nanocomposites showed higher photocatalytic activity under UV–vis light, because the existence of WO_3 is helpful to extend the optical absorption edge of ZnO from the ultraviolet to visible light region and inhibits the recombination of photoinduced carriers. The 40WZ nanocomposite had a MO dye removal efficiency of 100% with methyl orange within 15 min, which is far better than that of pure ZnO and WO_3.

Declaration of interest statement

We know of no conflicts of interest associated with this publication, and there has been no significant financial support for this work that could have influenced its outcome.

Data availability

The datasets used and/or analysed during the current study are available from the corresponding author on reasonable request.

Funding

No Funding.

References

1. Tchounwou, P.B., et al., Heavy metal toxicity and the environment. Exp Suppl, 2012. 101: p. 133-64.
2. Shabani, M., et al., Mesoporous-Mixed-Phase of Hierarchical Bismuth Oxychlorides Nanophotocatalyst with Enhanced Photocatalytic Application in Treatment of Antibiotic Effluents. Journal of Cleaner Production, 2018. 207.
3. Rajaram, T. and A. Das, Water pollution by industrial effluents in India: Discharge scenarios and case for participatory ecosystem specific local regulation. Futures, 2008. 40(1): p. 56-69.
4. Qu, X., P.J.J. Alvarez, and Q. Li, Applications of nanotechnology in water and wastewater treatment. Water Research, 2013. 47(12): p. 3931-3946.
5. Halder, J. and N. Islam, Water Pollution and its Impact on the Human Health. Journal of Environment and Human, 2015. 2: p. 36-46.
6. Chen, P., et al., Synchronous photosensitized degradation of methyl orange and methylene blue in water by visible-light irradiation. Journal of Molecular Liquids, 2021. 334: p. 116159.
7. Khoufi, S., F. Feki, and S. Sayadi, Detoxification of olive mill wastewater by electrocoagulation and sedimentation processes. J Hazard Mater, 2007. 142(1-2): p. 58-67.
8. Jiang, J.-Q., The role of coagulation in water treatment. Current Opinion in Chemical Engineering, 2015. 8: p. 36-44.
9. Lata, S. and S.R. Samadder, Removal of arsenic from water using nano adsorbents and challenges: A review. Journal of Environmental Management, 2016. 166: p. 387-406.
10. Gupta, V.K. and Suhas, Application of low-cost adsorbents for dye removal – A review. Journal of Environmental Management, 2009. 90(8): p. 2313-2342.
11. Avlonitis, S.A., et al., Simulated cotton dye effluents treatment and reuse by nanofiltration. Desalination, 2008. 221(1): p. 259-267.
12. Barragán, B.E., C. Costa, and M. Carmen Márquez, Biodegradation of azo dyes by bacteria inoculated on solid media. Dyes and Pigments, 2007. 75(1): p. 73-81.
13. Nasirian, M. and M. Mehrvar, Modification of TiO_2 to enhance photocatalytic degradation of organics in aqueous solutions. Journal of Environmental Chemical Engineering, 2016. 4(4, Part A): p. 4072-4082.
14. Kasimayan, U., et al., Enriched silver plasmon resonance activity on the sonochemical synthesis of ZnO flowers with α-Fe_2O_3 as an efficient catalyst for photo-Fenton reaction and photo-oxidation of ethanol. Journal of Water Process Engineering, 2019. 34: p. 101089.
15. Moniz, S.J.A., et al., Visible-light driven heterojunction photocatalysts for water splitting – a critical review. Energy & Environmental Science, 2015. 8(3): p. 731-759.
16. Qu, Y. and X. Duan, Progress, challenge and perspective of heterogeneous photocatalysts. Chemical Society Reviews, 2013. 42(7): p. 2568-2580.
17. Lei, R., et al., Novel ZnO nanoparticles modified WO_3 nanosheet arrays for enhanced photocatalytic properties under solar light illumination. Applied Surface Science, 2019. 463: p. 363-373.
18. Xie, J., et al., Simple preparation of WO_3–ZnO composites with UV–Vis photocatalytic activity and energy storage ability. Ceramics International, 2014. 40(8, Part A): p. 12519-12524.

19. Huang, X., et al., Single crystalline wurtzite ZnO/zinc blende ZnS coaxial heterojunctions and hollow zinc blende ZnS nanotubes: synthesis, structural characterization and optical properties. Nanoscale, 2014. 6(15): p. 8787-8795.
20. Chaudhary, K., et al., Binary WO_3-ZnO nanostructures supported rGO ternary nanocomposite for visible light driven photocatalytic degradation of methylene blue. Synthetic Metals, 2020. 269: p. 116526.
21. Pan, C. and Y. Zhu, A review of $BiPO_4$, a highly efficient oxyacid-type photocatalyst, used for environmental applications. Catalysis Science & Technology, 2015. 5(6): p. 3071-3083.
22. Lamba, R., et al., Well-crystalline porous ZnO–SnO_2 nanosheets: An effective visible-light driven photocatalyst and highly sensitive smart sensor material. Talanta, 2015. 131: p. 490-498.
23. Shakir, A., Silver nanoparticles as antimicrobial against salmonella typhi, proteus mirabilis and bacillus cereus as a model of gram - negative and cram - positive bacteria. World Journal of Pharmaceutical Research, 2016. 5: p. 49-55.
24. Boukrbiba, M., F. Sediri, and N. Gharbi, Hydrothermal synthesis of $WO_3 \cdot 1/3H_2O$ nanorods and study of their electrical properties. Polyhedron, 2010. 29: p. 2070-2074.
25. Subramani, T., et al., Surfactants assisted synthesis of WO_3 nanoparticles with improved photocatalytic and antibacterial activity: A strong impact of morphology. Inorganic Chemistry Communications, 2022. 142: p. 109709.
26. Mokhtar, H., et al., Photodegradation of Bisphenol A using WO_3/ZnO Photocatalyst under Visible Light Irradiation. Bioresources and Environment, 2023. 1: p. 54-64.
27. Yu, C., et al., Preparation of WO_3/ZnO Composite Photocatalyst and Its Photocatalytic Performance. Chinese Journal of Catalysis, 2011. 32(3): p. 555-565.
28. Adhikari, S., D. Sarkar, and G. Madras, Highly efficient WO_3-ZnO mixed oxides for photocatalysis. RSC Advances, 2015. 5.
29. Hunge, Y.M., et al., Photoelectrocatalytic degradation of phthalic acid using spray deposited stratified WO_3/ZnO thin films under sunlight illumination. Applied Surface Science, 2017. 420: p. 764-772.
30. Hunge, Y.M., A.A. Yadav, and V.L. Mathe, Ultrasound assisted synthesis of WO_3-ZnO nanocomposites for brilliant blue dye degradation. Ultrasonics Sonochemistry, 2018. 45: p. 116-122.
31. E, M., S. M.B, and J. P.E, Photocatalytic activity of ZnO-WO_3 for diclofenac degradation under visible light irradiation. Journal of Photochemistry and Photobiology A: Chemistry, 2019. 383: p. 111993.
32. Ghattavi, S. and A. Nezamzadeh-Ejhieh, A brief study on the boosted photocatalytic activity of AgI/WO_3/ZnO in the degradation of Methylene Blue under visible light irradiation. Desalination and Water Treatment, 2019. 166: p. 92-104.
33. Yasir, M., et al., ZnO nanowires and nanorods based ZnO/WO_3/Pt heterojunction for efficient photocatalytic degradation of estriol (E3) hormone. Materials Letters, 2022. 319: p. 132291.
34. Joudah Radhi, I., S.A. Hassan, and A.F. Alkaim, Preparation and Characterization of ZnO, WO_3/ZnO Nanocomposites Using Hydrothermal Method. Journal of Nanostructures, 2023. 13(4): p. 1133-1141.
35. Zhang, D., Z. Liu, and R. Mou, Preparation and characterization of WO_3/ZnO composite photocatalyst and its application for degradation of oxytetracycline in aqueous solution. Inorganic Chemistry Communications, 2022. 142: p. 109667.

36. Aziz, F., et al., Zinc oxide-tungsten oxide (ZnO-WO_3) composite for solar light-assisted degradation of organic dyes. Korean Journal of Chemical Engineering, 2023. 40(6): p. 1497-1509.
37. Alam, R., M.A. Hossain, and M. Elias, Amine functionalized graphene oxide decorated with ZnO-WO_3 nanocomposites for remediation of organic dye from wastewater. Journal of Physics and Chemistry of Solids, 2024. 190: p. 112015.
38. Faris, A.H., et al., Novel Mo-doped WO_3/ZnO nanocomposites loaded with polyvinyl alcohol towards efficient visible-light-driven photodegradation of methyl orange. Materials Letters, 2023. 334: p. 133746.
39. Rani, M., et al., Sunlight assisted highly efficient photocatalytic remediation of organic pollutants by green biosynthesized $ZnO@WO_3$ nanocomposite. Journal of Photochemistry and Photobiology A: Chemistry, 2024. 446: p. 115160.
40. Muneer, I., et al., Heterogeneous photocatalytic degradation of organic dyes by highly efficient $GdCoSnO_3$. Materials Science and Engineering: B, 2021. 265: p. 115028.
41. Nandiyanto, A.B.D., R. Zaen, and R. Oktiani, Correlation between crystallite size and photocatalytic performance of micrometer-sized monoclinic WO_3 particles. Arabian Journal of Chemistry, 2020. 13(1): p. 1283-1296.
42. He, L., et al., Investigation on the Mechanism and Inner Impetus of Photogenerated Charge Transfer in WO_3/ZnO Heterojunction Photocatalysts. The Journal of Physical Chemistry C, 2020. 124(51): p. 27916-27929.
43. Xu, Y. and T. Chen, Development of nanostructured based $ZnO@WO_3$ photocatalyst and its photocatalytic and electrochemical properties: Degradation of Rhodamine B. International Journal of Electrochemical Science, 2023. 18(4): p. 100055.
44. Ashiegbu, D. and H. Potgieter, ZnO-based heterojunction catalysts for the photocatalytic degradation of methyl orange dye. Heliyon, 2023. 9: p. e20674.
45. Xu, L., et al., ZnO with Different Morphologies Synthesized by Solvothermal Methods for Enhanced Photocatalytic Activity. Chemistry of Materials, 2009. 21(13): p. 2875-2885.
46. Li, B. and Y. Wang, Facile Synthesis and Enhanced Photocatalytic Performance of Flower-like ZnO Hierarchical Microstructures. Journal of Physical Chemistry C - J PHYS CHEM C, 2009. 114.
47. Vinayagam, R., et al., Synthesis, characterization and photocatalytic dye degradation capability of Calliandra haematocephala-mediated zinc oxide nanoflowers. Journal of Photochemistry and Photobiology B: Biology, 2020. 203: p. 111760.
48. Koohestani, H., A. Balooch, and H. Staji, Biosynthesis of CuO-nanoparticles using extracts of Mespilus germanica, Crataegus spp., and Wild barberry and their synergistic antibacterial activity. Giant, 2025: p. 100379.
49. Jalili, Z., R. Tayebee, and F.M. Zonoz, Eco-friendly synthesis of chromeno[4,3-b]chromenes with a new photosensitized WO_3/$ZnO@NH_2$-EY nanocatalyst. RSC Advances, 2021. 11(29): p. 18026-18039.
50. Ying, Y.L., et al., Structural and Antibacterial Properties of WO_3/ZnO Hybrid Particles against Pathogenic Bacteria. Materials Today: Proceedings, 2019. 17: p. 1008-1017.
51. Li, N., et al., WO_3-ZnO as an anti-gastric cancer agent and efficient photocatalyst in the synthesis of substituted benzimidazoles. Inorganic Chemistry Communications, 2024. 161: p. 112025.

52. Lam, S.M., et al., Sunlight responsive WO_3/ZnO nanorods for photocatalytic degradation and mineralization of chlorinated phenoxyacetic acid herbicides in water. J Colloid Interface Sci, 2015. 450: p. 34-44.
53. Subash, B. and R. Sasikala, High-performance photocatalytic and antibacterial properties of WO_3/ZnO honeycomb structures: synthesis and mechanistic insights. Journal of the Iranian Chemical Society, 2025. 22(4): p. 849-869.
54. Jafarabadi, A., M. Sobhani, and H. Koohestani, Fabrication and characterization of highly visible-light responsive TiO_2/Fe_2TiO_5 ceramic. Inorganic Chemistry Communications, 2023. 154: p. 111008.
55. Hunge, Y., A. Yadav, and V. Mathe, Ultrasound assisted synthesis of WO_3-ZnO nanocomposites for brilliant blue dye degradation. Ultrasonics Sonochemistry, 2018. 45.